Supplementary Information:

GeSn/SiGeSn Heterostructure and Multi Quantum Well Lasers

Daniela Stange[1*], Nils von den Driesch[1,2], Thomas Zabel[3], Francesco Armand-Pilon[3], Denis Rainko[1], Bahareh Marzban[4], Peter Zaumseil[5], Jean-Michel Hartmann[6], Zoran Ikonic[7], Giovanni Capellini[5,8], Siegfried Mantl[1], Hans Sigg[3], Jeremy Witzens[4], Detlev Grützmacher[1], and Dan Buca[1]

[1]*Peter Grünberg Institute (PGI 9) and JARA-Fundamentals of Future Information Technologies, Forschungszentrum Jülich, 52425 Jülich, Germany*

[2]*JARA-Institute Green IT, RWTH Aachen University, 52075 Aachen, Germany*

[3]*Laboratory for Micro- and Nanotechnology (LMN), Paul Scherrer Institute, CH-5232 Villigen, Switzerland*

[4]*Institute of Integrated Photonics and JARA-Fundamentals of Future Information Technologies, RWTH Aachen University, 52074 Aachen, Germany*

[5]*IHP, Im Technologiepark 25, 15236 Frankfurt (Oder), Germany*

[6]*Univ. Grenoble Alpes, CEA, LETI, F-38000 Grenoble, France*

[7]*Pollard Institute, School of Electronic and Electrical Engineering, University of Leeds, Leeds LS2 9JT, United Kingdom*

[8]*Department of Sciences, Università Roma Tre, 00146 Roma, Italy*

This file contains: 7 pages, 5 figures

Double Heterostructure- Material

A cross-section transmission electron micrograph (X-TEM) of the DHS comprising a 380 nm thick $Ge_{0.855}Sn_{0.145}$ active region sandwiched between 50 nm thick SiGeSn cladding layers is shown in Figure SI1. The double heterostructure incorporates GeSn with a higher Sn concentration as the GeSn buffer, on top of which it is grown. Therefore, a large strain builds up inside the heterostructure and the heterostructure unintentionally relaxes further after the critical thickness is exceeded. The misfit dislocations formed when relaxation takes place are located at the interface between the SiGeSn cladding and the GeSn active layer, which is detrimental for radiative recombination efficiency.

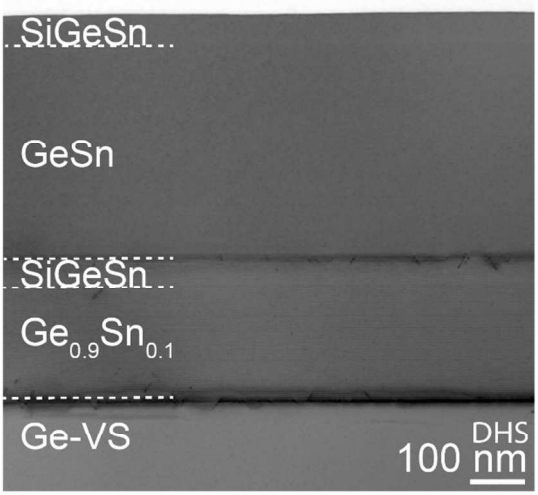

Figure S1 A TEM of the DHS structure reveals misfit dislocation at the interface between the SiGeSn bottom cladding and the active GeSn layer, which are generated by further strain relaxation of the heterostructure stack.

Carrier density calculation

The ratio of the carrier densities, discussed in Figure 2d of the main text, is evaluated as follows. For both layer stacks, a constant excitation power density of 3.4 kW/cm^2 is assumed for the 532 nm laser wavelength. This results in an average carrier density of ~$4 \cdot 10^{16}$ cm^{-3} inside the MQW and DHS epitaxial stacks, assuming recombination rates to be dominated by non-radiative recombination with a carrier lifetime of ~300 ps (and almost equal total stack thicknesses). Carrier concentrations are expected to be low enough for screening/band-bending effects to be neglected, i.e. the flat band condition is assumed. In addition, carriers are supposed to be at thermal equilibrium, with the associated electron and hole quasi-Fermi-levels $E_{fc,v}$, so that carrier concentrations averaged over the entire stacks are simply given by

$$n = \frac{1}{w} \sum_{\Gamma,L\ /\ HH,LH} \int \frac{\rho_{c,v}(E)dE}{1 + \exp[\pm \frac{E - E_{fc,v}}{k_B T}]}$$

and are equal for electrons and holes due to overall charge neutrality. Here, w is the total stack thickness, $\rho_{c,v}(E)$ is the local density of states for the conduction or valence bands in a given layer, k_B Boltzmann's constant and T the temperature. The integral is taken over the entire stack and the summation over all the relevant valleys, Γ, L for electrons and HH, LH for holes. In the first step, the quasi-Fermi-levels required to obtain the targeted average concentration are iteratively determined. In the second step, the carrier concentrations are determined in each of the valleys inside the active material. By repeating the calculation at different temperatures, the data required to generate the modeling curve in Figure 2d was obtained. As a final remark it should be noted that the relevant assumptions are the flat-band condition, carrier concentrations according to thermodynamic equilibrium relative to the quasi-Fermi levels, equal excitation densities and recombination rates dominated by similar dark recombination rates – the specific carrier concentrations in the above are only given to exemplify orders of magnitude.

Strain simulation

The calculated strain in the radial plane of the MQW-A microdisk is plotted in Figure SI2 for two different wells. The top well (orange) exhibits a higher degree of relaxation than the bottom well (blue), i.e. -0.05% vs. -0.2% residual compressive strain. This is due to elastic bending of the disk, stretching the top well more than the bottom well. In contrast to that, the regions directly above the pillar show a different behavior due to anchoring. The strongly varying strain values at the edges of the disk are calculation artefacts without any physical meaning.

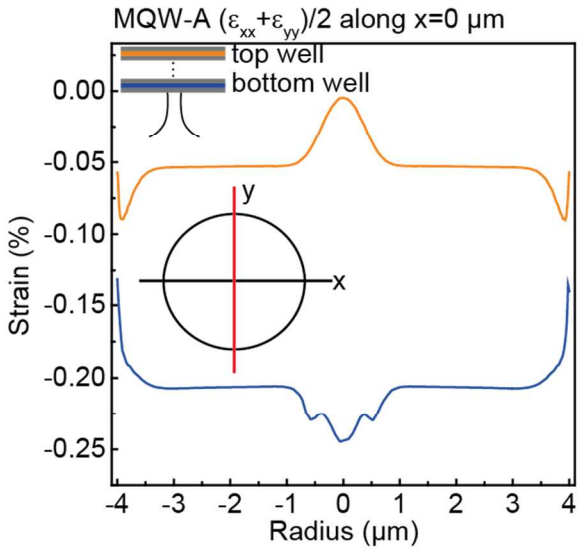

Figure S2 Distribution of ($\varepsilon_{xx}+\varepsilon_{yy}$)/2 strain component, along y (x=0) in the bottom and top wells of MQW-A microdisk. The red line shows the direction along which the strain was calculated.

Double Heterostructure- Lasing

The performance of a 8 μm diameter DHS microdisk laser, pumped at 1064 nm (Nd:YAG laser), is shown in Figure SI3. Lasing spectra taken at 20 K for different pump powers demonstrate the transitions from spontaneous emission to lasing and finally to spectrally multimode operation. The light-in light-out (L-L) characteristics are presented for three different temperatures in Figure SI4b. As shown previously[11,12,25], the slope efficiency of the GeSn laser sharply decreases as the temperature increases. For DHS, the threshold at 50 K is determined to be 250 kW/cm^2, which can also be seen in the emission spectrum collapse in Figure 4a. At about ~700 kW/cm^2, the slope efficiency of the L-L curve at 50 K markedly increases. This regime coincides with the onset of multi-mode operation in Figure 4a. At ~1000 kW/cm^2 the laser output power saturates due to thermal and band filling effects. In comparison to the bulk GeSn based laser structures reported earlier[14,25], the introduction of SiGeSn claddings does not appear to improve the lasing threshold excitation density. This undesirable result is partially ascribed to the fact that the (still existing) defective interface between the lower SiGeSn barrier and the active material, to which carriers inside the well are directly exposed, continues to contribute to non-radiative carrier recombination (NRCR). The generally higher threshold values reported for higher Sn content lasers in Ref.[25] and Ref.[14] indicate that the defect densities likely increase for increasing Sn concentrations. The L-L temperature characteristics for DHS shown in Figure SI4b indicate that the lasing ceases at a temperature of 120 K, since the linearity of the L-L curve throughout the whole range of pumping levels implies a spontaneous emission dominated luminescence. In line with threshold density values, the

maximum lasing temperature has not essentially improved in this heterostructure. These results suggest that other improvements paths such as 2D heterostructures have to be explored on the way towards more efficient lasing.

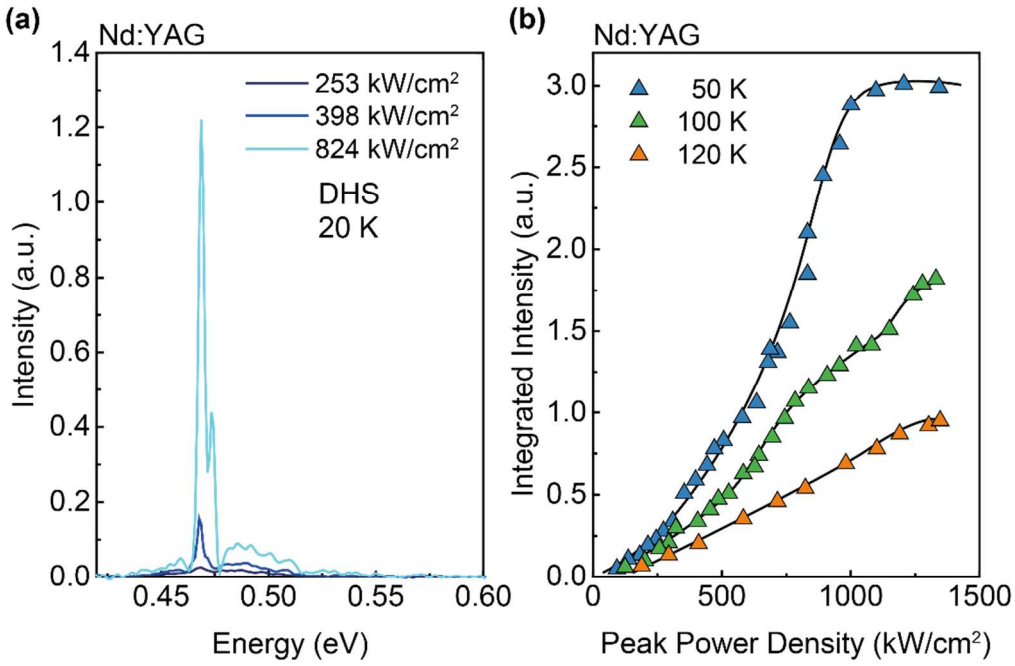

Figure S3 Emission characteristics of a DHS microdisk (8 µm diameter). **(a)** Spectra for increasing pumping powers showing spontaneous emission lasing near threshold and multimode lasing at high pump power, respectively. **(b)** Light-in light-out curves taken at three different temperatures. The Nd:YAG laser pumping was used for (a) and (b).

Threshold determinations

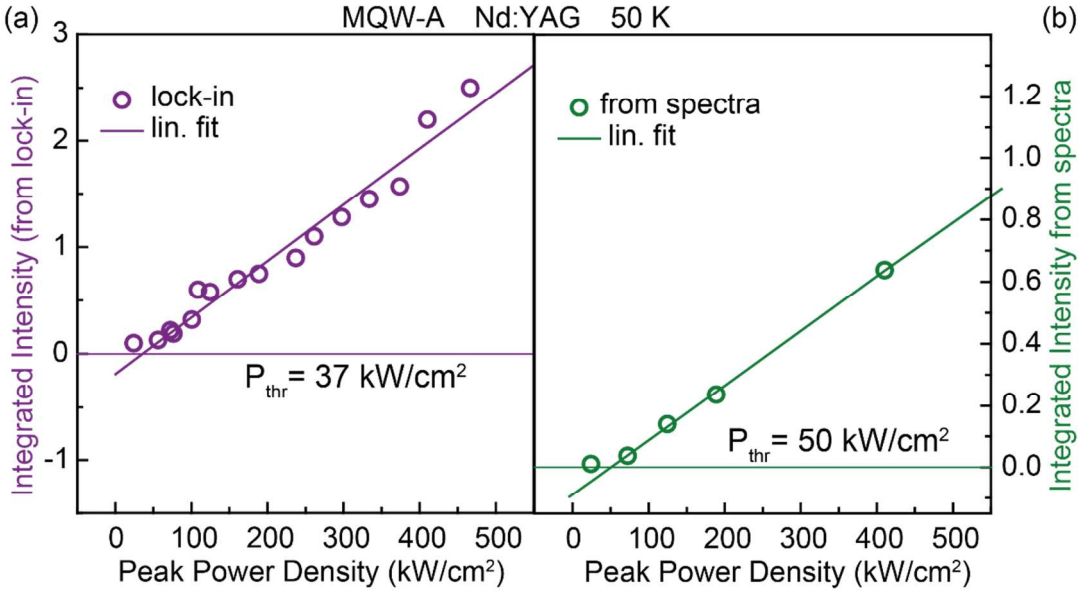

Figure S4 Linear fit for threshold determination from two different data sets: the integrated emission intensity obtained by the lock-in amplifier (in (a) purple) and obtained from the recorded spectra (in (b) green), both measured at 50 K with Nd:YAG pumping.

A straight line is fitted to (i) values obtained directly by the lock-in amplifier (purple data points, Figure SI4a) and (ii) the emission intensity obtained from the integration of individual spectra (green data points, Figure SI4b) at the same temperature and for the same device at pumping powers around the lasing onset. The threshold value is determined by the intersection of the fit with the abscissa. The average of both values is given in the manuscript as threshold while their difference is given as the measurement uncertainty. Combining both, a lasing threshold of (43 ± 7) kW/cm^2 peak power density at 50 K is extracted.

Laser spot size determination

The laser spot size of the excitation lasers is used to determine the peak power densities used in the manuscript. Therefore, the error on this determination influences the extracted threshold values. In the following the determination procedure is described.

The laser power is measured with a power meter close to the sample position, while a razorblade is driven through the laser spot at the sample position with a resolution of 1 µm steps. The resulting intensity profile is plotted in figure SI5a.

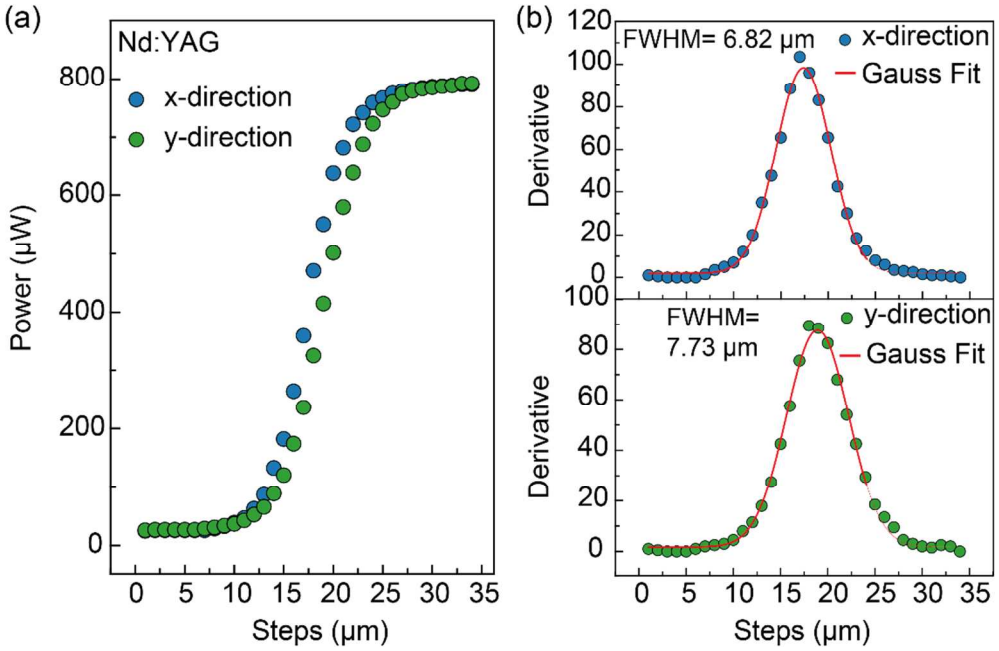

Figure S5 Intensity profile of the excitation spot of the Nd:YAG laser in the horizontal and vertical directions (a). The derivative of this profile shows a Gaussian beam (b).

With the derivative of this data, the Gaussian beam profile can be fitted in the x- (horizontal) as well as in the y-direction (vertical). The beam size is determined as the FWHM of the Gauss function and the mean value of the x- and y- directions is taken as spot diameter, assuming a circular excitation spot geometry. In the case of Nd:YAG excitation, the spot diameter is determined to be (7.3±0.2) µm, while the spot size for excitation with 1550 nm is determined in the same manner and results in (6.9±0.7) µm.